

Coherent Phonon-Driven Band Renormalizations in $1T'$ -MoTe₂

Carl E. Jensen,^{1, a)} Christoph Emeis,² Stephan Jauernik,¹ Petra Hein,¹ Fabio Caruso,² and Michael Bauer^{1, 3, b)}

¹⁾*Institute of Experimental and Applied Physics, Kiel University, 24118 Kiel, Germany*

²⁾*Institute of Theoretical Physics and Astrophysics, Kiel University, 24118 Kiel, Germany*

³⁾*Kiel Nano, Surface and Interface Science KiNSIS, Kiel University, 24118 Kiel, Germany*

(Dated: 24 February 2026)

Here, we investigate phonon mode- and electron band-selective electron–phonon couplings in centrosymmetric $1T'$ -MoTe₂ using time- and angle-resolved photoemission spectroscopy combined with frequency-domain analysis. Femtosecond near-infrared pulses excite coherent A_g -symmetric phonon modes at 2.34 THz, 3.34 THz, and 3.86 THz, which manifest as oscillatory modulations in photoemission intensity and binding energy across the valence bands. Pixel-wise Fourier analysis using recently developed methodologies reveals pronounced band selectivity with distinct coupling strengths for different electronic states and phonon modes, enabling the evaluation of band-renormalization amplitudes in the range of few meV. *Ab initio* calculations qualitatively reproduce the experimentally observed coupling patterns and relative trends, demonstrating the capability of combined experimental and theoretical approaches to resolve ultrafast electron–phonon interactions in quantum materials.

INTRODUCTION

Transition metal dichalcogenides (TMDCs) have emerged as a versatile platform for exploring novel quantum phenomena due to their rich polymorphism and tunable electronic properties^{1,2}. Among the TMDCs, molybdenum ditelluride (MoTe₂) is of particular interest, as it hosts a variety of crystal phases with distinct topological and electronic characteristics. These include semiconducting, semimetallic, Weyl-semimetallic, and superconducting phases^{3,4}, making MoTe₂ a promising candidate for future quantum electronic and optoelectronic applications.

In this material, coherent phonons and their coupling to electronic degrees of freedom are of particular interest, as they can drive structural phase transitions and thus enable ultrafast control of the associated electronic properties through optical excitation. Examples include a transient phase transition from the topologically non-trivial Td phase to the topologically trivial $1T'$ phase of MoTe₂ through coherent excitation of a low-frequency shear mode⁵, and the prediction of a phase transition from the semiconducting $2H$ -phase to the semimetallic $1T'$ phase of monolayer MoTe₂ through a complex interplay of different coherently excited phonon modes⁶.

Time- and angle-resolved photoemission spectroscopy (tr-ARPES) is a powerful tool for directly investigating the ultrafast dynamics of electronic excitations and their coupling to phonons^{7–9}. Furthermore, tr-ARPES allows the observation of changes in the electronic band structure due to coupling to coherent phonons¹⁰. A phonon frequency-selective analysis of these data (frequency do-

main ARPES – FDARPES) enables a mode-specific projection of the electron-phonon interaction onto the measured electronic band structure^{11,12}.

In this work, we employ tr-ARPES and FDARPES to investigate phonon mode and electron band-resolved electron–phonon interactions in $1T'$ -MoTe₂. A near infrared femtosecond laser pulse launches the excitation of several coherent phonon modes, whose signatures are observed as oscillatory modulations in the photoemission intensity and binding energy of electronic bands. Our FDARPES analysis reveals a pronounced selectivity in the coupling between specific bands and the A_g -symmetric phonon modes at $\nu_1 = 2.34$ THz, $\nu_2 = 3.34$ THz, and $\nu_3 = 3.86$ THz. In a recent study of the related compound WTe₂ in the Td phase an analysis method was presented that makes it possible to disentangle the various causes of such oscillations and quantify their amplitudes¹³. Application of this method to our photoemission data allows us to quantitatively extract amplitudes of observed band renormalizations that arise from changes in the wave function overlap and the screening behavior within the crystal lattice as the electronic potential landscape is modulated by the periodic ionic displacements.

In addition, we performed *ab initio* calculations of coherent phonon-driven band renormalizations in $1T'$ -MoTe₂, which we analyze in analogy to the experimental data. In a direct comparison, we find good qualitative agreement between experiment and theory. Possible causes for observed quantitative deviations include a potential systematic underestimation of excitation amplitudes by the evaluation method applied to the experimental data and uncertainties regarding the photoexcitation density.

^{a)}Electronic mail: cjensen@physik.uni-kiel.de

^{b)}<https://www.physik.uni-kiel.de/de/institute/ag-bauer>

METHODS

$1T'$ -MoTe₂ single crystals (2D Semiconductors), were mounted on a tantalum sample holder using a two-component epoxy. A cleaving post was affixed to the crystal surface with the same epoxy, and the sample was subsequently cleaved in ultrahigh vacuum ($\leq 2 \cdot 10^{-10}$ mbar). Tr-ARPES measurements were performed using a pump-probe scheme as schematically illustrated in Fig. 1(a). Near-infrared (NIR) p-polarized pump pulses at 837 nm (1.5 eV) were used for excitation at an absorbed fluence of $\approx 0.3 \text{ mJ/cm}^2$. The response of the electronic system to the photoexcitation was probed using time-delayed and s-polarized near-ultraviolet (NUV) pulses at 210 nm (5.9 eV). The time resolution was determined to be 130 fs corresponding to the full width at half maximum of the NIR-NUV cross-correlation signal. The emitted photoelectrons were detected using a hemispherical electron energy analyzer. All experiments were performed at room temperature. More details about the experimental setup can be found in¹⁴.

The electronic band structure, phonon dispersions, and electron-phonon coupling (EPC) matrix elements were determined using density functional theory (DFT) and density functional perturbation theory (DFPT). The time-dependent electronic distribution function $f_{n\mathbf{k}}(t)$ and the coherent lattice displacements $Q_\nu(t)$ are obtained by solving the time-dependent Boltzmann equations and the coherent-phonon equation of motion. Our first principles simulations were conducted using the open-source computer codes Quantum ESPRESSO^{15,16} and EPW¹⁷. Further information on the theory and the computational details can be found in¹⁸ and in the supplementary information¹⁹, respectively.

RESULTS AND DISCUSSION

MoTe₂ belongs to the family of TMDCs. Its crystal structure consists of weakly coupled layers held together by van der Waals interactions. At room temperature, MoTe₂ adopts the centrosymmetric, monoclinic $1T'$ phase. Its crystal structure and Brillouin zone are shown in Figs. 1(b) and 1(c), respectively. The left panel of Fig. 1(d) compares experimental ARPES data of $1T'$ -MoTe₂ and the result of a DFT band structure calculation (dashed lines) along the Γ -X high-symmetry direction. Both experimental data and the results of the band structure calculations agree well with the results of previous work^{20,21}. The right panel of Fig. 1(d) shows the spectral function calculated from the DFT band structure under consideration of electron-phonon interaction in a many-body framework. Overall, experimental data and calculations agree well, in particular in the binding energy range between the Fermi level E_F and -0.4 eV . We assign differences between experiment and calculations, such as the clear discrepancy in spectral weight near Γ , to effects such as the coupling to final state reso-

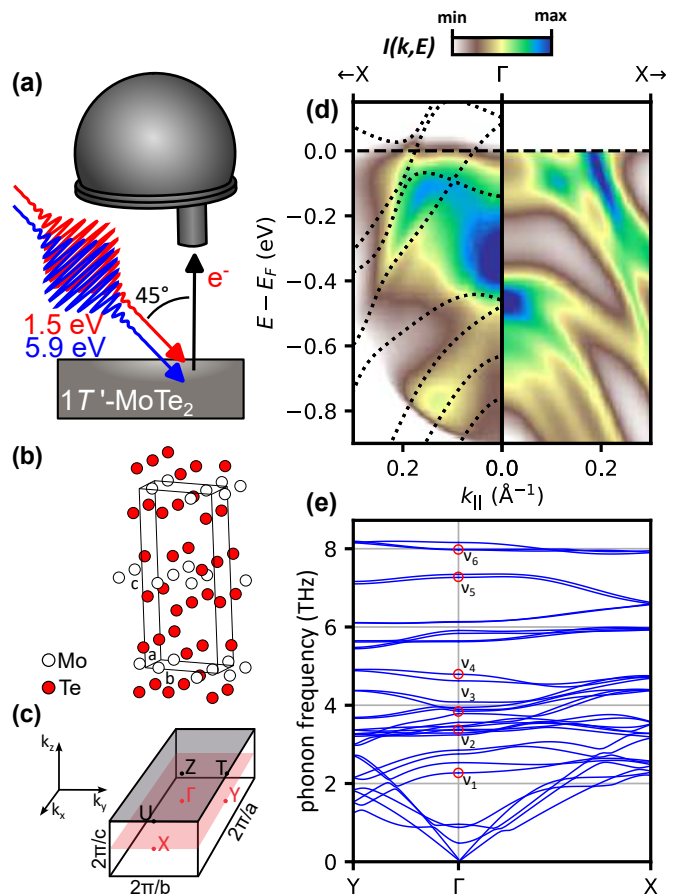


FIG. 1. (a) Schematic illustration of the tr-ARPES experiment. (b) Crystal structure of $1T'$ -MoTe₂. (c) First Brillouin zone of $1T'$ -MoTe₂ with high symmetry points indicated. (d) Room-temperature ARPES spectrum at $h\nu = 5.9 \text{ eV}$ (left panel) and spectral function calculated from the DFT band structure (right panel) along the Γ -X direction. The experimental data is overlaid with the DFT band structure (dashed lines). k_{\parallel} denotes the electron wave vector parallel to the sample surface. (e) Calculated phonon dispersions of $1T'$ -MoTe₂. A_g -symmetric phonon modes that are coherently excited and observed in the experiment are marked in red.

nances or a possible k_z -offset, at which the 5.9 eV photons probe the electronic structure with respect to the Γ -X-Y plane. In a photoemission study of the related compound WTe₂, we have discussed the origins of these differences in more detail¹¹. Further differences may arise from surface states and resonances in the ARPES data that are not considered in the first principle calculations²².

Figure 1(e) shows the phonon dispersions of $1T'$ -MoTe₂ along the Γ -X and Γ -Y directions, calculated using DFPT. The A_g -symmetric phonon modes marked in red are relevant for the analysis of the tr-ARPES data. In previous time-resolved all-optical studies, the coherent excitation of these modes was experimentally demonstrated^{23,24}.

Figure 2(a) presents tr-ARPES data of $1T'$ -MoTe₂ recorded 1.5 ps after excitation by the pump pulse. To isolate the transient response of the electronic system

upon photoexcitation, a reference spectrum recorded prior to excitation was subtracted from the raw data. Blue regions indicate a loss of spectral weight compared to the state before excitation, while red regions indicate a gain. The areas highlighted in green, red, and turquoise mark spectral regions of three different electronic bands identified in the ARPES spectrum that will be referred to as 'band 1', 'band 2', and 'band 3' in the following. Figure 2(b) shows difference energy distribution curves (EDC) at $k_{\parallel} \approx 0.18 \text{ \AA}^{-1}$ [see gray marked area in Fig. 2(a)] as a function of pump-probe delay Δt . The gain in spectral weight above E_F and part of the initial loss of spectral weight below E_F indicate photoexcitation of charge carriers due to the absorption of the near-infrared (NIR) pump pulse.

We observe additional changes in the spectral weight distribution that are clear signatures of laser-induced dynamics in the electronic system beyond pure charge carrier dynamics. This applies in particular to the increase in spectral weight in some regions below E_F and the pronounced time-periodic changes observable on time scales $\Delta t \gtrsim 1 \text{ ps}$. Such oscillatory behavior in the electronic structure is a typical indication of the excitation of coherent phonons that couple to the electronic system through strong electron-phonon interaction. It is precisely these changes that will be the focus of the following data analysis and discussion.

Figure 2(c) displays the integral photoemission intensities as a function of Δt extracted from the three regions of interest (ROI) marked in Fig. 2(a), each covering the response of a distinct electronic band. In the graph, we have disregarded data for $\Delta t < 1 \text{ ps}$, as the transient signal is dominated by the charge carrier dynamics in this time range. All three transients exhibit clear oscillatory behavior. Contributions from different oscillation periods can be seen in the data, with the relative amplitudes varying among the bands.

An analysis using a fast Fourier transform (FFT) allows us to resolve the different frequency contributions to the photoemission intensity transients. Prior to FFT analysis, the transients were background-corrected using a polynomial fit to remove non-oscillatory components associated with charge carrier population dynamics. Details of the analysis can be found in the supplemental information¹⁹. The FFT results are shown in Fig. 2(d). Overall, we observe six spectral peaks at $\nu_1 = 2.34 \text{ THz}$, $\nu_2 = 3.34 \text{ THz}$, $\nu_3 = 3.86 \text{ THz}$, $\nu_4 = 4.81 \text{ THz}$, $\nu_5 = 7.25 \text{ THz}$ and $\nu_6 = 7.78 \text{ THz}$. These frequencies match the frequencies of the six A_g -symmetric phonon modes marked in Fig. 1(e) quite reasonably and show very good agreement with the results of other time-resolved studies of MoTe_2 ^{23–29}.

Each band has a characteristic spectral fingerprint. The data of band 1 shows a dominance of the ν_1 mode, while the amplitudes of ν_2 and ν_3 are greatly reduced in comparison. The signal for band 2 suggests a strong coupling to ν_2 in the selected energy-momentum region, while ν_1 and ν_3 are significantly weaker in amplitude. For this

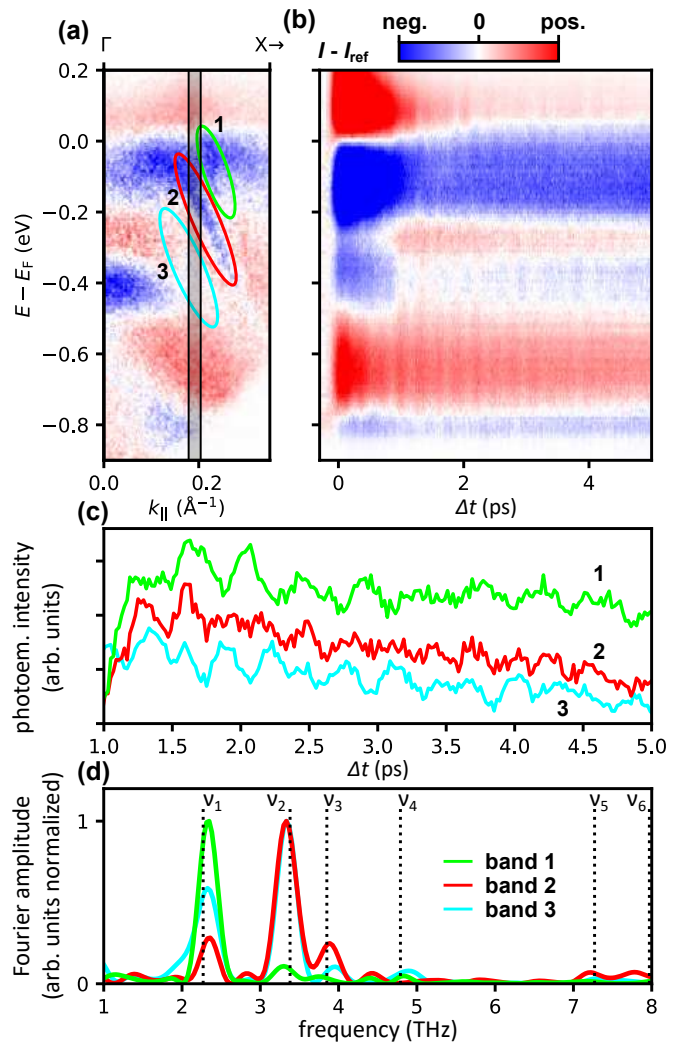


FIG. 2. (a) Tr-ARPES spectrum along Γ -X at $\Delta t = 1.5 \text{ ps}$. To highlight the nonequilibrium response to photoexcitation, a tr-ARPES spectrum recorded at negative Δt has been subtracted from the raw data. Red (blue) regions denote gain (loss) of spectral weight relative to the equilibrium state. The ROIs marked in green, red, and turquoise indicate different electronic bands. (b) Difference EDCs at $k_{\parallel} \approx 0.18 \text{ \AA}^{-1}$ as a function of Δt . The grey shaded area marked in (a) indicates the momentum range that was used for integration. The oscillations in photoemission hint to the excitation of coherent phonons. (c) Transient integral photoemission intensities for $\Delta t > 1 \text{ ps}$ from the three ROIs marked in (a). (d) Normalized Fourier spectra of the transients in (c), revealing band-specific couplings to different coherent phonon modes.

band, we also observe small amplitudes near ν_5 and ν_6 . In the case of band 3 ν_2 is again the strongest mode, but the relative coupling to ν_1 is notably enhanced compared to band 2. In addition, the small signal at ν_3 and ν_4 could also indicate weak coupling to these modes.

To further explore the band-selectivity of EPC in $1T'$ - MoTe_2 , we employ the FDARPES method for data analysis^{11,30–32}. In this method, the tr-ARPES data is

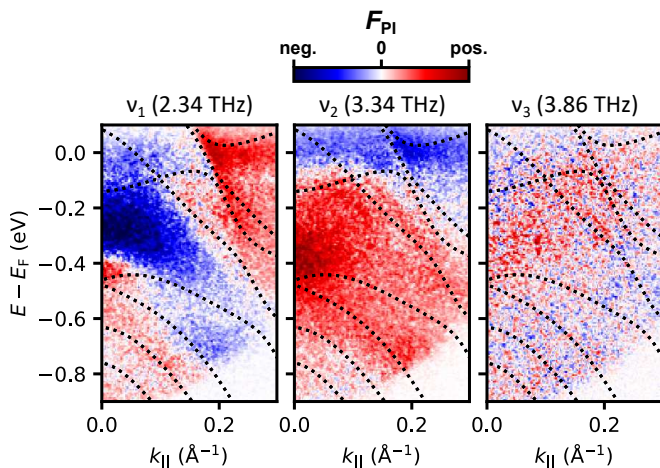


FIG. 3. FDARPES maps for the three coherent phonon modes (ν_1 , ν_2 , ν_3) dominating the electronic response. The data are overlaid with DFT band structures for comparison (dashed lines). The color intensity is a measure of the Fourier amplitude, while the color coding represents its sign, so that both strength and phase of the response of the electronic system to the phonon excitation are depicted.

subjected to a pixel-by-pixel Fourier analysis. This enables an intuitive and phonon mode-specific representation of the electronic response due to EPC.

Figure 3 compares results of such an analysis for the frequency components ν_1 , ν_2 , and ν_3 , i.e., for the three low-frequency phonon modes that are identified in the tr-ARPES data. Details on data analysis are described in the supplementary information¹⁹. The data (in the following referred to as FDARPES maps) show for a selected phonon mode ν_i the real part of the Fourier component F_{PI} as a function of electron energy E and wave vector k . Here, the Fourier amplitude is represented by the color intensity, while the relative phase of the photoemission response in the different regions is encoded in the blue-red contrast, which indicates a phase difference of π or close to π .

Comparison of the FDARPES maps reveals pronounced differences in both phase and amplitude patterns implying that the different phonon modes couple very differently to the electronic states, similar to previous results for the related compound $Td\text{-WTe}_2$ ^{11,13}. In addition, when compared to the DFT band structure (dashed lines) the electronic bands can in some areas be traced in the FDARPES maps rather well and often separate regions of opposite phase response. The dispersive contours are partly even better visible than in the ARPES spectrum in Fig. 1(d).

The oscillations in the photoemission intensities that are encoded for each phonon mode in the FDARPES maps via F_{PI} can have different origins¹³. This includes (i) oscillations in the band energies (band renormalizations), (ii) oscillations of the integral spectral weight, e.g., as a result of changes in the photoemission matrix element, and (iii) oscillations of the band-intrinsic

linewidths. In general, these contributions superimpose each other in the Fourier signal. Using an elaborated analysis method described in detail in Ref.¹³, it is possible to partially separate the different contributions in the spectra. In the following, we will apply the analysis procedure to our data that is referred in¹³ to as photoemission intensity analysis (PI analysis) focusing specifically on band renormalizations due to coherent phonon excitations.

Contributions to F_{PI} due to time-dependent band renormalizations $\delta E(t)$ can be directly related to the derivative of the static ARPES intensity $I(k, E)$ with respect to energy E , $\partial I(k, E)/\partial E$. For a sufficiently small renormalization amplitude ΔE , the photoemission intensity can be expanded as $I(k, E + \delta E(t)) \approx I(k, E) + \delta E(t)\partial_E I(k, E)$, so that, to first order, the Fourier component at the phonon frequency is given by³³

$$F_{\text{PI}} \approx -\Delta E \times \frac{\partial I(k, E)}{\partial E}. \quad (1)$$

The equation implies that, for an isolated band, this contribution to F_{PI} is antisymmetric with respect to the energy band position and has a zero crossing at this energy.

If F_{PI} originates from oscillations in spectral weight it can be written as

$$F_{\text{PI}} = \Delta SW \times I(k, E), \quad (2)$$

with ΔSW being the amplitude of the spectral weight oscillation. This contribution to F_{PI} is symmetric with respect to the energy band position and shows a maximum at this energy.

There is no similarly simple analytic relation between F_{PI} describing an oscillation in the linewidth. However, as is the case of spectral weight oscillations, this contribution is symmetric with respect to the energy band position and shows a maximum at this energy¹³.

The characteristic spectral shapes of the three contributions make it possible to partly distinguish them in the FDARPES maps. Furthermore, Eq. 1 can be used to quantify energy shifts ΔE due to band renormalizations.

Figures 4(a)–(c) compare a static ARPES spectrum $I(k, E)$ of $1T'\text{-MoTe}_2$, its derivative $\partial I(k, E)/\partial E$, and the FDARPES map for ν_1 within a selected energy-momentum window. Furthermore, Figs. 4(d) and 4(e) compare the normalized momentum-integrated profiles from the purple and green marked ROIs A and B in Figs. 4(a)–(c).

In ROI A [Fig. 4(d)], we focus on the energy range between E_{F} and $E - E_{\text{F}} = -0.2$ eV. Here, both F_{PI} and $\partial I(k, E)/\partial E$ show matching zero crossings, indicating a proportionality according to Eq. (1) and thus an energy shift ΔE due to a band renormalization. The zero crossing simultaneously marks the energy band position (see above) and indeed coincides with a maximum in $I(k, E)$.

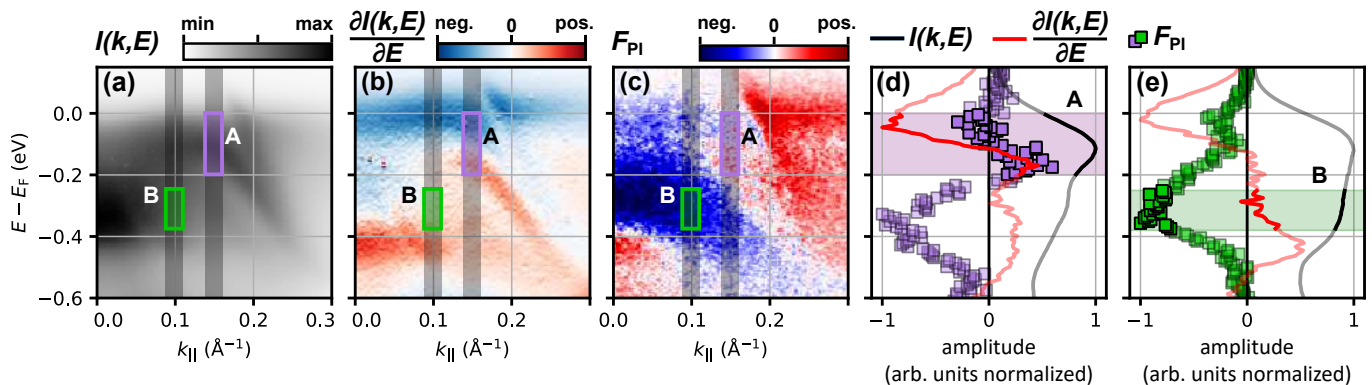


FIG. 4. (a) Selected energy-momentum region of the ARPES data $I(k, E)$ shown in Fig. 1(d). (b) Energy gradient $\partial I(k, E)/\partial E$ as a function of energy and momentum of the data shown in (a). (c) FDARPES map for the ν_1 mode in the energy-momentum region covered by the ARPES data in (a). (d), (e) Comparison of $I(k, E)$, $\partial I(k, E)/\partial E$, and F_{PI} along the grey shaded areas marked in Figs. (a)–(c). The discussion in the text focuses on ROI A (d) and B (e) marked in purple and green. All data in (d) and (e) are normalized to their maximum value.

This explains why the calculated band dispersions in the FDARPES maps in Fig. 3 tend to trace boundaries separating regions of opposite phase.

In region B [Fig. 4(e)], F_{PI} shows no zero crossing. Instead, we observe that within the energy range $-0.35 \text{ eV} \lesssim E - E_F \lesssim -0.25 \text{ eV}$ highlighted in green F_{PI} shows a distinct maximum that coincides with the low energy maximum in the double peak structure of $I(k, E)$. This indicates dominance of spectral-weight or linewidth oscillations in this region. Outside this window F_{PI} cannot be clearly assigned to either $I(k, E)$ or $\partial I(k, E)/\partial E$, suggesting a superposition of different contributions or overlapping bands.

Overall, this comparison highlights the complexity of the EPC landscape captured by our FDARPES data of $1T'$ - MoTe_2 and demonstrates that interpreting the origin of the Fourier signal requires a careful, region-specific analysis as outlined in detail in Ref.¹³.

To gain quantitative information on the band energy shifts ΔE due to band renormalizations, we perform a linear regression between the F_{PI} signal and $\partial I(k, E)/\partial E$ using sliding windows across the full FDARPES maps (PI analysis). According to Eq. 1, the regression slope directly yields ΔE . We performed a PI analysis for the data for ν_1 and ν_2 . Due to the low overall contrast in the FDARPES map [see Fig. 3(c)] such an analysis did not deliver meaningful results for ν_3 . A helpful tool supporting the PI analysis is the so-called first-moment analysis (FM analysis). As shown in Ref.¹³, in an FM analysis the influence of spectral weight oscillations are suppressed, allowing band renormalizations to be identified by comparing the energy and momentum dependence of the FM analysis to the results of the PI analysis. Details of the FM analysis of our data are described in the supplementary information¹⁹

Additionally we performed calculations using the *ab initio* framework described in the methods section under consideration of the experimental excitation parameters. The calculations generate time- and momentum-resolved

spectral functions in which only the phonon-induced band renormalizations are taken into account. To enable the direct comparison, the theory results are finally analyzed in the same way as the experimental data.

Figure 5 compares the PI-analyzed experimental data [(a), (d)] and the PI-analyzed results of the *ab initio* calculations [(b), (e)] for the two phonon modes ν_1 and ν_2 . The direct theoretical band renormalizations from the *ab initio* calculations visualized along the DFT band structure are shown in Figs. 5 (c) and (f). To isolate the band-specific response in the experimental data, we exploit phase boundaries in the FDARPES maps as band-position markers. An edge detection filter identifies these boundaries, generating masks that restrict the evaluation of ΔE and its appearance in Figs. 5 (a) and (d) to the band structure detected in the experiment (see¹⁹). The displayed color intensity is a measure of the amplitude of the band renormalization ΔE , while the color coding represents the sign of ΔE at time zero, i.e., the initial direction of the band renormalization.

In the experimental data we select ROIs A–D [see markings in Figs. 5(a) and 5(b)], based on a qualitative agreement of the PI analysis data with the FM analysis data^{13,19}. Matching ROIs are marked in the PI-analyzed theory data in Figs. 5(c) and 5(d). The match was ensured by choosing identical momentum ranges and adjusting the energy ranges according to the differences in the experimental and theoretical band structures.

Overall, we observe for both modes a very good qualitative agreement between the PI-analyzed experimental and theory data. The ν_1 mode shows particular strong band renormalizations in ROIs A and D with initial energy shifts in opposite directions. In ROI C, both experiment and theory hint to a phase reversal at $\approx 0.19 \text{ \AA}^{-1}$. Its origin could stem from an avoided crossing of two bands in this region, indicated by the dashed lines. The apparent discrepancy between experiment and theory in the initial sign of the band renormalization in ROI B

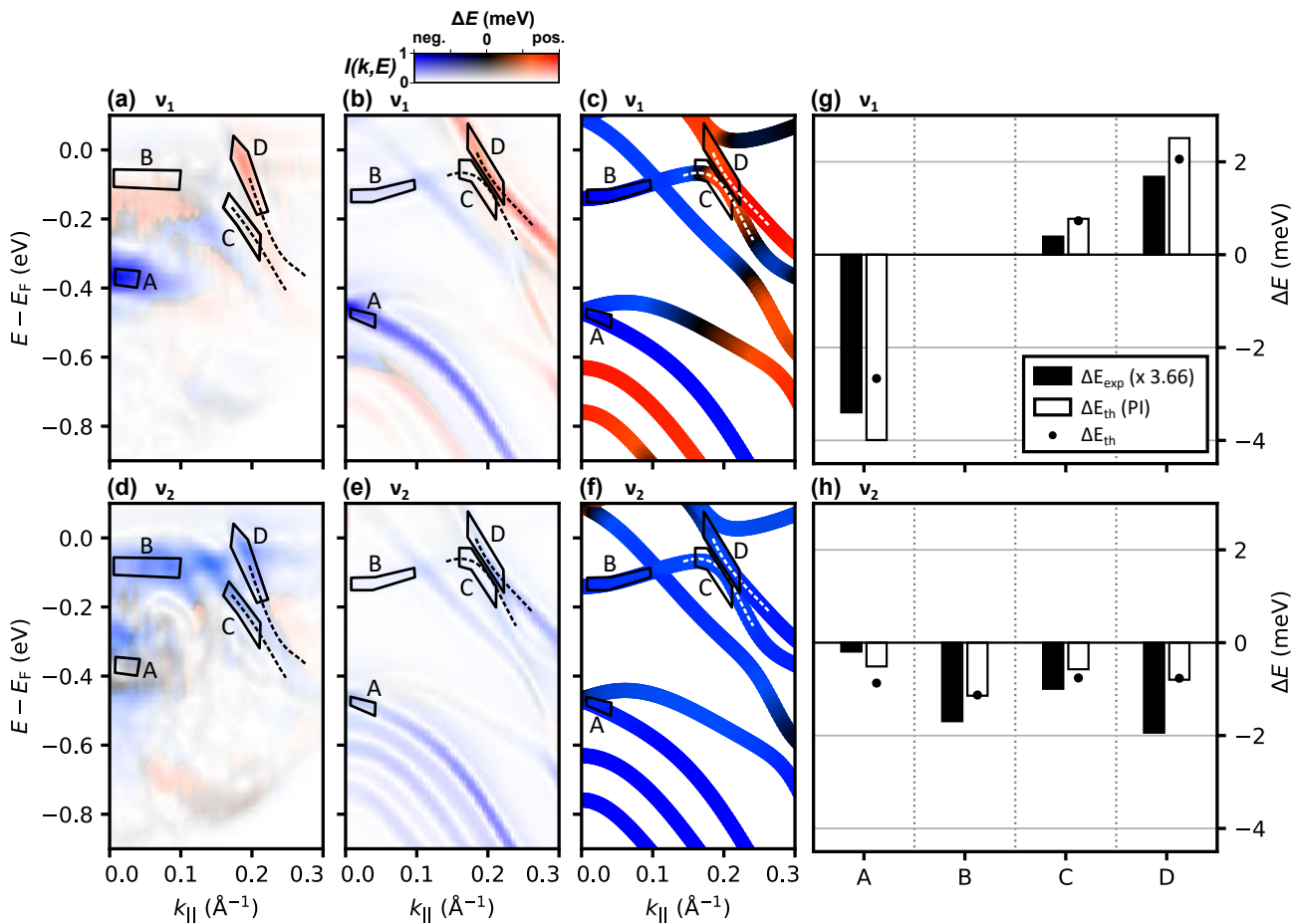


FIG. 5. (a), (d) Results of the PI analysis of the experimental data for ν_1 (a) and ν_2 (d). (b), (e) Corresponding results of the PI analysis of the theory data for comparison. (c), (f) *ab initio* data of the band renormalization used to generate the data shown in (b) and (e). The dashed lines in the figures indicate an avoided crossing in the band structure as deduced from the band structure mask determined from the experimental FDARPES data [(a), (d)] and the DFT band structure [(b), (c), (e), (f)]. The evaluated energy shifts ΔE due to band renormalizations are superimposed with a mask derived from an edge detection applied to the corresponding FDARPES maps and the photoemission intensity to highlight only contributions to the data near or in the vicinity of electronic bands. The five ROIs (A–D) marked in (a)–(f) indicate different electronic bands. (g), (h) Amplitudes of ΔE , determined from the respective average value in the ROIs A–E in (a) and (d) as well as (c) and (f). The experimental values are scaled with the mean ratio between the experimental and theoretical values. Black points show the *ab initio* values of the amplitudes in the ROIs displayed (c) and (f).

appears to be due to a signal contribution in the experimental data from the high binding energy region below ROI B. We associate the finite signal amplitude in this energy region with $\partial I(k, E)/\partial E$ being very close to zero [cf. Fig. 4 (b)]. This leads to a significant and erroneous signal enhancement according to equation (1). We assume that this signal, which we cannot be related to a band, is an artifact of the analysis procedure. It will not be considered in the further discussion.

For the ν_2 mode, experiment and theory show for all four ROIs a good agreement regarding the initial sign of band renormalization and the relative renormalization amplitudes. Furthermore, experiment and theory also agree qualitatively regarding the comparison of the relative amplitudes between ν_1 and ν_2 .

For a quantitative comparison, we determined the

renormalization amplitudes ΔE for ROIs A–D by signal averaging over the respective ROI. The experimental and calculated values for ΔE are of the same order of magnitude, but the experiment systematically yields smaller amplitudes than the theory. Experimental renormalization amplitudes range between 0.05 meV and 0.9 meV. Very similar values have been reported for similar excitation conditions for the related compound WTe_2 ¹³. The theory yields renormalization amplitudes between 0.5 meV and 4.0 meV.

A direct comparison of the renormalization amplitudes for ROI A–D is shown in Fig. 5(e). Here, the experimental data are scaled by a factor of 3.66, the average of the ratio between calculated and experimental ΔE for the four ROIs. In addition to the theory values extracted from the PI-analyzed data, we also added the actual *ab initio* values for ΔE [(Fig. 5(c) and (f))] to the graph

(black dots). This data representation confirms the very good match between experiment and theory regarding the relative amplitudes of the band renormalizations in the different ROIs and their initial sign. Interestingly, we observe a substantial quantitative deviation between the theory value derived from the PI-analyzed data and the actual *ab initio* value for ROI A. According to theory, in this area two bands overlap. This indicates that in such a scenario, a PI-analysis yields quantitatively inaccurate values in accordance with findings reported in Ref.¹³.

The systematic deviation between experimental and calculated renormalization amplitudes can have various causes: The tendency of a systematic underestimation of excitation amplitudes by the evaluation method as reported in¹³, the possible k_z -offset in the experimental photoemission data with respect to the Γ -X-Y plane considered in the theory, and typical uncertainties in determining absorbed excitation fluence. Finally, residual spectral-weight or linewidth contributions to the experimental data cannot be completely excluded.

CONCLUSION

In summary, we have demonstrated the band-selectivity of coherent phonon-driven band renormalizations in the semimetal $1T'$ -MoTe₂. The frequency-domain ARPES (FDARPES) method reveals insights into the mode-selective response of the electronic structure to the excitation of coherent phonons.

The application of a recently introduced PI analysis method delivers quantitative results on amplitude and initial direction of coherent phonon-driven band renormalizations, while the FM analysis is used to strengthen the robustness of the interpretation¹³. For an excitation density in the few 100 $\mu\text{J}/\text{cm}^2$ range we observe in the experiment typical renormalization amplitudes of a few 100 μeV for different bands and the two phonon modes at frequencies $\nu_1 = 2.34$ THz and $\nu_2 = 3.34$ THz that dominate the electronic structure response in this material. *Ab initio* calculations reproduce the initial directions of band renormalization for both ν_1 and ν_2 remarkably well. The calculated amplitudes of band renormalizations are of the same order of magnitude as in the experiment, but systematically higher. The overall very good qualitative agreement between theory and experiment suggests that such work will enable further insights into electron-phonon coupling phenomena in quantum materials in the future, thanks to recent developments in the methods used to evaluate such experimental data^{11,13} and the parallel advances made in the theoretical description of these phenomena¹⁸.

ACKNOWLEDGMENTS

This work is funded by the Deutsche Forschungsgemeinschaft (DFG), Projects No. 443988403 and No.

499426961. The authors gratefully acknowledge the computing time provided by the high-performance computer Lichtenberg at the NHR Centers NHR4CES at TU Darmstadt (Project p0021280).

DATA AVAILABILITY

The experimental data that support the findings of this study are openly available on Zenodo at <http://doi.org/10.5281/zenodo.18671857>.

The theory data that support the findings of this study are openly available in the NOMAD database at <http://doi.org/10.17172/NOMAD/2026.02.19-3>.

AUTHOR DECLARATIONS

Conflict of Interest

The authors have no conflicts to disclose.

Author Contributions

Carl E. Jensen and Michael Bauer conceived the experiments. Carl E. Jensen and Stephan Jauernik carried out the experiments. Carl E. Jensen and Petra Hein performed the data analysis. Christoph Emeis performed the calculations. All authors contributed to the scientific discussion. Carl E. Jensen, Christoph Emeis, Fabio Caruso, and Michael Bauer cowrote the paper.

¹S. Manzeli, D. Ovchinnikov, D. Pasquier, O. V. Yazyev, and A. Kis, "2D transition metal dichalcogenides," *Nat. Rev. Mater.* **2** (2017), 10.1038/natrevmats.2017.33.

²M. Chhowalla, H. S. Shin, G. Eda, L. J. Li, K. P. Loh, and H. Zhang, "The chemistry of two-dimensional layered transition metal dichalcogenide nanosheets," *Nat. Chem.* **5**, 263–275 (2013).

³Y. Qi, P. G. Naumov, M. N. Ali, C. R. Rajamathi, W. Schnelle, O. Barkalov, M. Hanfland, S. C. Wu, C. Shekhar, Y. Sun, V. Süß, M. Schmidt, U. Schwarz, E. Pippel, P. Werner, R. Hillebrand, T. Förster, E. Kampert, S. Parkin, R. J. Cava, C. Felser, B. Yan, and S. A. Medvedev, "Superconductivity in Weyl semimetal candidate MoTe₂," *Nat. Commun.* **7**, 1–7 (2016), arXiv:1508.03502.

⁴K. Deng, G. Wan, P. Deng, K. Zhang, S. Ding, E. Wang, M. Yan, H. Huang, H. Zhang, Z. Xu, J. Denlinger, A. Fedorov, H. Yang, W. Duan, H. Yao, Y. Wu, S. Fan, H. Zhang, X. Chen, and S. Zhou, "Experimental observation of topological Fermi arcs in type-II Weyl semimetal MoTe₂," *Nat. Phys.* **12**, 1105–1110 (2016), arXiv:1603.08508.

⁵M. Y. Zhang, Z. X. Wang, Y. N. Li, L. Y. Shi, D. Wu, T. Lin, S. J. Zhang, Y. Q. Liu, Q. M. Liu, J. Wang, T. Dong, and N. L. Wang, "Light-induced subpicosecond lattice symmetry switch in mote₂," *Phys. Rev. X* **9**, 021036 (2019).

⁶M. X. Guan, X. B. Liu, D. Q. Chen, X. Y. Li, Y. P. Qi, Q. Yang, P. W. You, and S. Meng, "Optical Control of Multistage Phase Transition via Phonon Coupling in," *Phys. Rev. Lett.* **128**, 15702 (2022).

⁷L. Perfetti, P. a. Loukakos, M. Lisowski, U. Bovensiepen, H. Eisaki, and M. Wolf, "Ultrafast electron relaxation in superconducting $bi_2sr_2cacu_2o_{8+\delta}$ by time-resolved photoelectron spectroscopy," *Phys. Rev. Lett.* **99**, 197001 (2007).

- ⁸J. C. Johannsen, S. Ulstrup, F. Cilento, A. Crepaldi, M. Zacchigna, C. Cacho, I. C. E. Turcu, E. Springate, F. Fromm, C. Roidel, T. Seyller, F. Parmigiani, M. Grioni, and P. Hofmann, “Direct view of hot carrier dynamics in graphene,” *Phys. Rev. Lett.* **111**, 027403 (2013).
- ⁹A. Stange, C. Sohr, L. X. Yang, G. Rohde, K. Janssen, P. Hein, L.-P. Oloff, K. Hanff, K. Rossnagel, and M. Bauer, “Hot electron cooling in graphite: Supercollision versus hot phonon decay,” *Phys. Rev. B* **92**, 184303 (2015).
- ¹⁰L. Perfetti, P. A. Loukakos, M. Lisowski, U. Bovensiepen, H. Berger, S. Biermann, P. S. Cornaglia, A. Georges, and M. Wolf, “Time evolution of the electronic structure of $1t$ - TaS_2 through the insulator-metal transition,” *Phys. Rev. Lett.* **97**, 067402 (2006).
- ¹¹P. Hein, S. Jauernik, H. Erk, L. Yang, Y. Qi, Y. Sun, C. Felser, and M. Bauer, “Mode-resolved reciprocal space mapping of electron-phonon interaction in the weyl semimetal candidate $1t$ - WTe_2 ,” *Nature communications* **11**, 2613 (2020).
- ¹²U. De Giovannini, H. Hübener, S. A. Sato, and A. Rubio, “Direct Measurement of Electron-Phonon Coupling with Time-Resolved ARPES,” *Phys. Rev. Lett.* **125**, 136401 (2020), arXiv:2004.11082.
- ¹³N. Gauthier, H. Soifer, J. A. Sobota, H. Pfau, E. J. Sie, A. M. Lindenberg, Z.-X. Shen, and P. S. Kirchmann, “Analysis methodology of coherent oscillations in time- and angle-resolved photoemission spectroscopy,” *Review of Scientific Instruments* **96** (2025).
- ¹⁴S. Jauernik, P. Hein, M. Gurgel, J. Falke, and M. Bauer, “Probing long-range structural order in snpc/ag (111) by umklapp process assisted low-energy angle-resolved photoelectron spectroscopy,” *Physical Review B* **97**, 125413 (2018).
- ¹⁵P. Giannozzi, S. Baroni, N. Bonini, M. Calandra, R. Car, C. Cavazzoni, D. Ceresoli, G. L. Chiarotti, M. Cococcioni, I. Dabo, *et al.*, “Quantum ESPRESSO: a modular and open-source software project for quantum simulations of materials,” *J. Phys. Condens. Matter* **21**, 395502 (2009).
- ¹⁶P. Giannozzi, O. Andreussi, T. Brumme, O. Bunau, M. B. Nardelli, M. Calandra, R. Car, C. Cavazzoni, D. Ceresoli, M. Cococcioni, *et al.*, “Advanced capabilities for materials modelling with Quantum ESPRESSO,” *J. Phys. Condens. Matter* **29**, 465901 (2017).
- ¹⁷H. Lee, S. Poncé, K. Bushick, S. Hajinazar, J. Lafuente-Bartolome, J. Leveillee, C. Lian, J.-M. Lihm, F. Macheda, H. Mori, *et al.*, “Electron-phonon physics from first principles using the EPW code,” *npj Computational Materials* **9**, 156 (2023).
- ¹⁸C. Emeis, S. Jauernik, S. Dahiya, Y. Pan, C. E. Jensen, P. Hein, M. Bauer, and F. Caruso, “Coherent phonons and quasiparticle renormalization in semimetals from first principles,” *Physical Review X* **15**, 021039 (2025).
- ¹⁹See Supplemental Material at [URL will be inserted by publisher] for additional information with citations to Refs^{34–46}.
- ²⁰A. Crepaldi, G. Autès, A. Sterzi, G. Manzoni, M. Zacchigna, F. Cilento, I. Vobornik, J. Fujii, P. Bugnon, A. Magrez, H. Berger, F. Parmigiani, O. V. Yazyev, and M. Grioni, “Persistence of a surface state arc in the topologically trivial phase of mote_2 ,” *Phys. Rev. B* **95**, 041408 (2017).
- ²¹J. Park, A. N. Batyrkhanov, J. Brandhoff, F. Otto, M. Grunewald, M. Schaal, S. Hus, T. Fritz, F. Goltl, A.-P. Li, *et al.*, “Lifshitz transition and band structure evolution in alkali metal intercalated $1t$ - mote_2 ,” *The Journal of Physical Chemistry C* **129**, 5065–5074 (2025).
- ²²A. Damascelli, “Probing the electronic structure of complex systems by arpes,” *Physica Scripta* **2004**, 61 (2004).
- ²³T. Fukuda, K. Makino, Y. Saito, P. Fons, A. V. Kolobov, K. Ueno, and M. Hase, “Ultrafast dynamics of the low frequency shear phonon in $1t$ - mote_2 ,” *Applied physics letters* **116** (2020).
- ²⁴M. Zhang, Z. Wang, Y. Li, L. Shi, D. Wu, T. Lin, S. Zhang, Y. Liu, Q. Liu, J. Wang, *et al.*, “Light-induced subpicosecond lattice symmetry switch in mote_2 ,” *Physical Review X* **9**, 021036 (2019).
- ²⁵K. Zhang, C. Bao, Q. Gu, X. Ren, H. Zhang, K. Deng, Y. Wu, Y. Li, J. Feng, and S. Zhou, “Raman signatures of inversion symmetry breaking and structural phase transition in type-ii weyl semimetal mote_2 ,” *Nature communications* **7**, 13552 (2016).
- ²⁶S.-Y. Chen, T. Goldstein, D. Venkataraman, A. Ramasubramanian, and J. Yan, “Activation of new raman modes by inversion symmetry breaking in type ii weyl semimetal candidate $1t$ - mote_2 ,” *Nano letters* **16**, 5852–5860 (2016).
- ²⁷R. Beams, L. G. Cançado, S. Krylyuk, I. Kalish, B. Kalanyan, A. K. Singh, K. Choudhary, A. Bruma, P. M. Vora, F. Tavazza, *et al.*, “Characterization of few-layer $1t$ - mote_2 by polarization-resolved second harmonic generation and raman scattering,” *ACS nano* **10**, 9626–9636 (2016).
- ²⁸X. Ma, P. Guo, C. Yi, Q. Yu, A. Zhang, J. Ji, Y. Tian, F. Jin, Y. Wang, K. Liu, *et al.*, “Raman scattering in the transition-metal dichalcogenides of $1t$ - mote_2 , td-mote_2 , and td-wt e_2 ,” *Physical Review B* **94**, 214105 (2016).
- ²⁹J. Lai, X. Liu, J. Ma, Q. Wang, K. Zhang, X. Ren, Y. Liu, Q. Gu, X. Zhuo, W. Lu, *et al.*, “Anisotropic broadband photoresponse of layered type-ii weyl semimetal mote_2 ,” *Advanced materials* **30**, 1707152 (2018).
- ³⁰T. Suzuki, Y. Shinohara, Y. Lu, M. Watanabe, J. Xu, K. L. Ishikawa, H. Takagi, M. Nohara, N. Katayama, H. Sawa, M. Fujisawa, T. Kanai, J. Itatani, T. Mizokawa, S. Shin, and K. Okazaki, “Detecting electron-phonon coupling during photo-induced phase transition,” *Phys. Rev. B* **103**, L121105 (2021).
- ³¹W. Lee, S. Fernandez-Mulligan, H. Tan, C. Yan, Y. Guan, S. H. Lee, R. Mei, C. Liu, B. Yan, Z. Mao, and S. Yang, “Layer-by-layer disentanglement of Bloch states,” *Nat. Phys.* **19**, 950–955 (2023).
- ³²Q. Ren, T. Suzuki, T. Kanai, J. Itatani, S. Shin, and K. Okazaki, “Phase-resolved frequency-domain analysis of the photoemission spectra for photoexcited $1T$ - TaS_2 in the Mott insulating charge density wave state,” *Appl. Phys. Lett.* **122** (2023), 10.1063/5.0149692.
- ³³U. De Giovannini, H. Hübener, S. A. Sato, and A. Rubio, “Direct measurement of electron-phonon coupling with time-resolved arpes,” *Physical Review Letters* **125**, 136401 (2020).
- ³⁴I. Sobel, “An isotropic 3×3 image gradient operator,” Presentation at Stanford A.I. Project 1968 (2014).
- ³⁵F. Caruso and D. Novko, “Ultrafast dynamics of electrons and phonons: from the two-temperature model to the time-dependent boltzmann equation,” *Advances in Physics: X* **7**, 2095925 (2022).
- ³⁶Y. Pan and F. Caruso, “Vibrational dichroism of chiral valley phonons,” *Nano Letters* **23**, 7463–7469 (2023).
- ³⁷F. Caruso and M. Zacharias, “Quantum theory of light-driven coherent lattice dynamics,” *Phys. Rev. B* **107**, 054102 (2023).
- ³⁸F. Giustino, “Electron-phonon interactions from first principles,” *Rev. Mod. Phys.* **89**, 015003 (2017).
- ³⁹A. Dal Corso, “Pseudopotentials periodic table: From H to Pu,” *Comput. Mater. Sci.* **95**, 337–350 (2014).
- ⁴⁰J. P. Perdew, A. Ruzsinszky, G. I. Csonka, O. A. Vydrov, G. E. Scuseria, L. A. Constantin, X. Zhou, and K. Burke, “Restoring the density-gradient expansion for exchange in solids and surfaces,” *Phys. Rev. Lett.* **100**, 136406 (2008).
- ⁴¹H. J. Monkhorst and J. D. Pack, “Special points for brillouin-zone integrations,” *Phys. Rev. B* **13**, 5188–5192 (1976).
- ⁴²E. Bosoni, L. Beal, M. Bercx, P. Blaha, S. Blügel, J. Brüder, M. Callsen, S. Cottenier, A. Degomme, V. Dikan, *et al.*, “How to verify the precision of density-functional-theory implementations via reproducible and universal workflows,” *Nature Reviews Physics* **6**, 45–58 (2024).
- ⁴³B. E. Brown, “The crystal structures of wte_2 and high-temperature mote_2 ,” *Acta Crystallographica* **20**, 268–274 (1966).
- ⁴⁴S. Baroni, S. De Gironcoli, A. Dal Corso, and P. Giannozzi, “Phonons and related crystal properties from density-functional perturbation theory,” *Reviews of Modern Physics* **73**, 515 (2001).
- ⁴⁵N. Marzari, A. A. Mostofi, J. R. Yates, I. Souza, and D. Vanderbilt, “Maximally localized Wannier functions: Theory and applications,” *Reviews of Modern Physics* **84**, 1419–1475 (2012).

⁴⁶G. Pizzi, V. Vitale, R. Arita, S. Blügel, F. Freimuth, G. Géranton, M. Gibertini, D. Gresch, C. Johnson, T. Koret-

sune, *et al.*, “**Wannier90** as a community code: new features and applications,” *Journal of Physics: Condensed Matter* **32**, 165902 (2020).

Supplementary Materials for “Coherent Phonon-Driven Band Renormalizations in $1T'$ -MoTe₂”

Carl E. Jensen,^{1,*} Christoph Emeis,² Stephan Jauernik,¹

Petra Hein,¹ Fabio Caruso,² and Michael Bauer^{1,3,†}

¹*Institute of Experimental and Applied Physics,
Kiel University, 24118 Kiel, Germany*

²*Institute of Theoretical Physics and Astrophysics,
Kiel University, 24118 Kiel, Germany*

³*Kiel Nano, Surface and Interface Science KiNSIS,
Kiel University, 24118 Kiel, Germany*

(Dated: February 24, 2026)

Supplementary Note S1. GENERATION OF FDARPES MAPS

FDARPES maps are generated from the tr-ARPES data as follows: For $\Delta t \lesssim 800$ fs the transient changes observed in the tr-ARPES data are dominated largely by charge carrier dynamics. To isolate the oscillatory component of the signal from this signal contribution we omit all data for time delays $\Delta t < 810$ fs for further evaluation. In the following, the transient photoemission signal from each pixel of the tr-ARPES maps is considered separately. First, fifth-order polynomials are fitted to and subtracted from the transients to account for the low-frequency background of the data. Next, these transients are zero-padded to three times of their original length to increase the frequency resolution of the Fourier signal. The resulting transients are Fourier transformed and compiled into FDARPES maps, which provide the energy- and momentum-dependence of the Fourier signal for each frequency. In a final step, the Fourier signals are scaled by a factor of $\frac{2}{N}$ with N being the number of sampling values. This procedure restores the correct magnitude of the oscillation amplitude, which is crucial for the further quantitative analysis, such as the PI analysis.

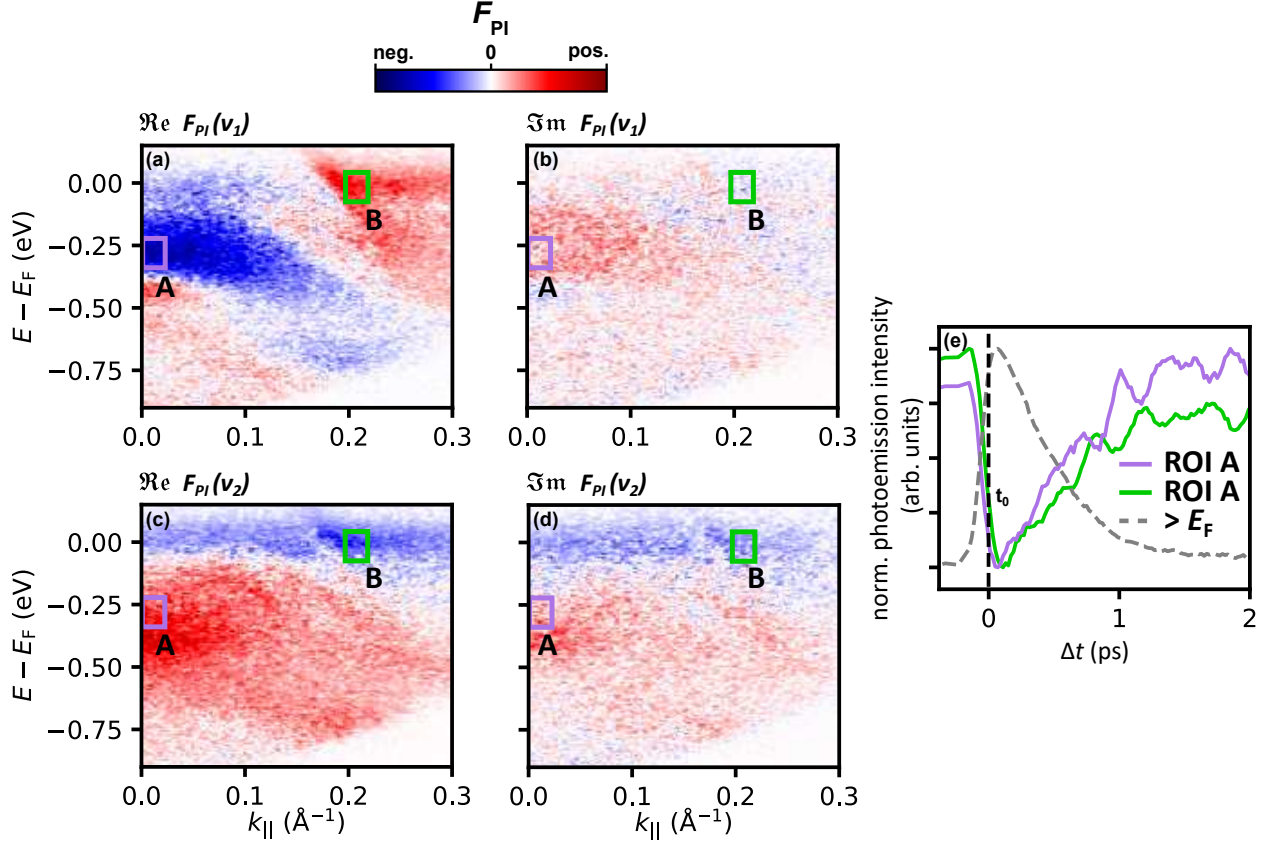
Supplementary Note S2. DETERMINING A GLOBAL TIME ZERO

For the PI and the FM analysis, an effective and common time zero t_0 for the launch of ν_1 and ν_2 must be determined. Two boundary conditions must be observed: i) Either imaginary part or real part of the Fourier components $F_{\text{PI}}(k, E)$ must be minimized simultaneously for ν_1 and ν_2 [1]. ii) t_0 must lie within the initial rise of the nascent carrier population generated in the photoabsorption process.

For our analysis we chose t_0 so that the imaginary part of $F_{\text{PI}}(k, E)$ is minimized. Fig. **S1** compares the real part [(a) and (c)] and imaginary part [(b) and (d)] of $F_{\text{PI}}(k, E)$ at t_0 for ν_1 and ν_2 , respectively. We suspect that the limited time resolution of the experiment (130 fs) and an incomplete subtraction of signal background are responsible for the residual signal visible in the imaginary part of the Fourier component. Fig. **S1** (e) shows the transient photoemission signal from the two regions of interest (ROI) A and B marked in Fig. **S1** (a)–(d) in comparison to the charge carrier population dynamics at an excitation energy $E - E_{\text{F}} \approx$ (grey dashed line), confirming that t_0 lies within the initial rise of the photoexcited nascent

* cjensen@physik.uni-kiel.de

† <https://www.physik.uni-kiel.de/de/institute/ag-bauer>



Supplementary Figure S1. (a)–(d) Real (\Re) and imaginary (\Im) part of $F_{PI}(k, E)$ for ν_1 (a,b) and ν_2 (c,d). (e) Transient photoemission signal from ROIs A and B in comparison to a photoemission intensity transient at $E - E_F \approx$ representing the temporal evolution of the photoexcited nascent electron population.

electron population.

Supplementary Note S3. GENERATION OF BAND STRUCTURE MASKS

To correlate the evaluated band renormalizations with the electronic band structure, it is important to determine the band positions based on the experimental photoemission data. In Ref. [1] this is achieved by determining the two-dimensional curvature of the photoemission intensity. Here, we take a different approach and use a fingerprint of the electronic band positions in the FDARPES maps [2]. Fig. S2(a) shows the simulation of an example electronic band with parabolic dispersion. To account for coupling to a coherent phonon mode, the band position is periodically modulated with an amplitude 0.1 eV in

energy direction. The corresponding FDARPES map is shown in Fig. **S2(b)**. The actual band position is captured in this data by the zero crossing of the Fourier signal separating the blue and red regions. Such boundary lines are also clearly visible in the experimental data in Fig. 3. A filter based on this signature can therefore further increase the sensitivity to band renormalization effects. To generate a band structure mask for the analysis of band renormalizations, we track this feature by applying a Sobel filter to the FDARPES map [3]. To avoid artifacts from signal noise in the experimental data, we apply a Gaussian blur before filtering.

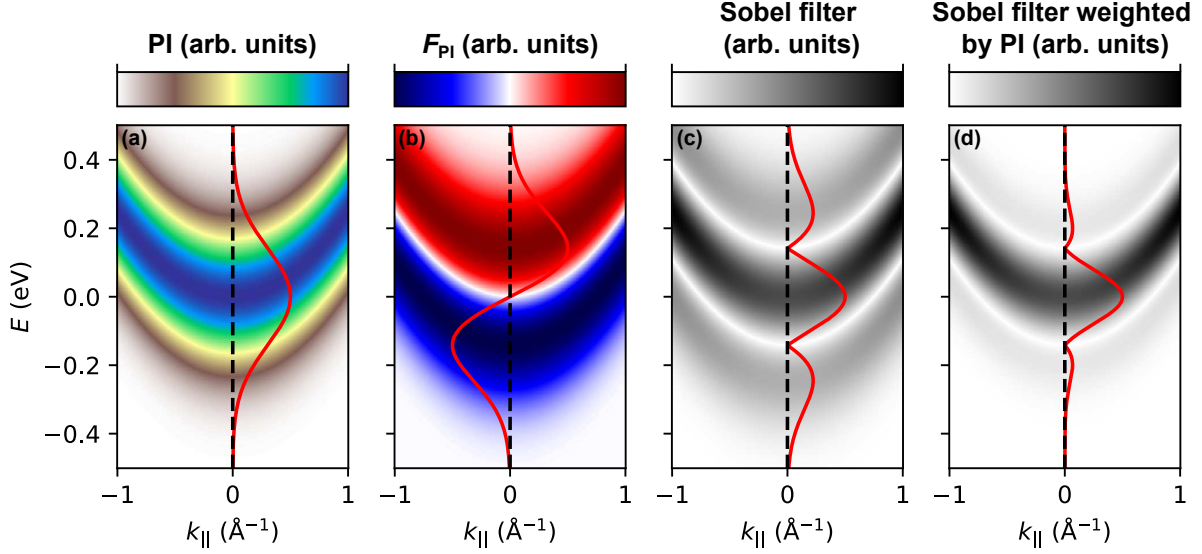
The filtered image of Fig. **S2(b)** is shown in Fig. **S2(c)**. The red line shows the intensity profile along the dashed line. The intensity is maximum at the actual band position, but secondary maxima appear above and below it. To suppress these artifacts, we multiply the filtered image with the photoemission intensity of the ARPES spectrum, resulting in the band structure mask shown in Fig. **S2(d)**. Fig. **S3** shows the masks used to generate Figs. 5(a) and 5(b) in the main text, calculated from the experimental FDARPES data for the phonon modes ν_1 and ν_2 . The ROIs from the main text are marked. Solid lines indicate that the ROI is chosen on the basis of the respective mask.

Supplementary Note S4. FIRST MOMENT (FM) ANALYSIS

To quantify band renormalizations from the experimental data, we apply the photoemission intensity (PI) analysis method to the experimental data, which is described in detail in Ref. [1]. An alternative method presented in the same study is based on a first moment (FM) analysis of the energy distribution curves of the tr-ARPES spectra. The quantitative validity of this method is less reliable, however, it is sensitive exclusively to band renormalization effects. It can therefore be used as a benchmark to clearly identify band renormalizations in the PI analysis data. The FM of an energy distribution curve I is given by [1]:

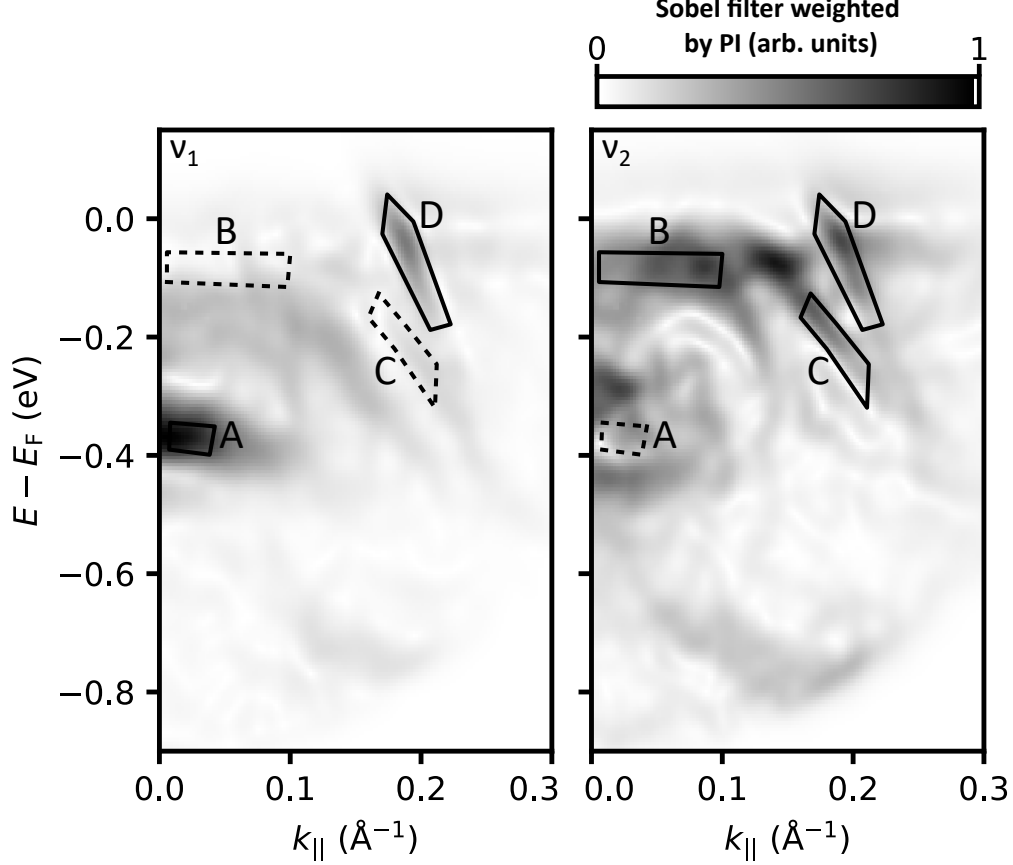
$$\text{FM}(k, E, t) = \frac{\int_{E-\delta/2}^{E+\delta/2} I(E', k, t) E' dE'}{\int_{E-\delta/2}^{E+\delta/2} I(E', k, t) dE'} \quad (\text{S1})$$

It is calculated pixel-by-pixel using a sliding window function with the window size $\delta = 0.2$ eV. For the following Fourier transform, the time-dependent incoherent background is subtracted by fitting a fifth-order polynomial to the transient FM of each pixel. The size of



Supplementary Figure S2. (a) Example of an electronic band to illustrate the method used to generate a band structure mask. For the following analysis the band energy is periodically modulated with an amplitude of 0.1 eV. (b) FDARPES map of the data shown in (a) for the chosen modulation frequency. (c) FDARPES map after application of a Sobel edge detection filter. (d) Band structure mask generated from multiplying Fig. (c) with the normalized photoemission intensity shown in (a). The red lines in (a)–(d) show the respective signal amplitude along the black dashed line.

the Fourier components directly reflect the band renormalization amplitude in this analysis. Fig. S4 compares the results of the PI analysis and the FM analysis of the experimental data for ν_1 and ν_2 . Over a large part of the spectrum and for both phonon frequencies we observe a very good qualitative agreement between the results of the two analysis methods with respect to the sign of ΔE . Relevant deviations can only be observed in two areas, which are marked by arrows. At a binding energy of $E - E_F \approx -0.45$ eV and near Γ , the PI and FM data show an opposite sign of ΔE for both ν_1 and ν_2 . At $E - E_F \approx -0.25$ eV and $k_{\parallel} \approx 0.15 \text{ \AA}^{-1}$ we observe an analogous difference for ν_1 . The origin for these deviations are most likely contributions from spectral weight or linewidth oscillations, which only affect the result of the PI analysis. These spectral regions are therefore not taken into account for the comparison of experimental and calculated band renormalizations.



Supplementary Figure S3. Band structure masks created by applying the described edge detection method to the experimental FDARPES data for ν_1 and ν_2 . ROIs from mentioned in the main text are marked.

Supplementary Note S5. THEORY AND COMPUTATIONAL METHODS

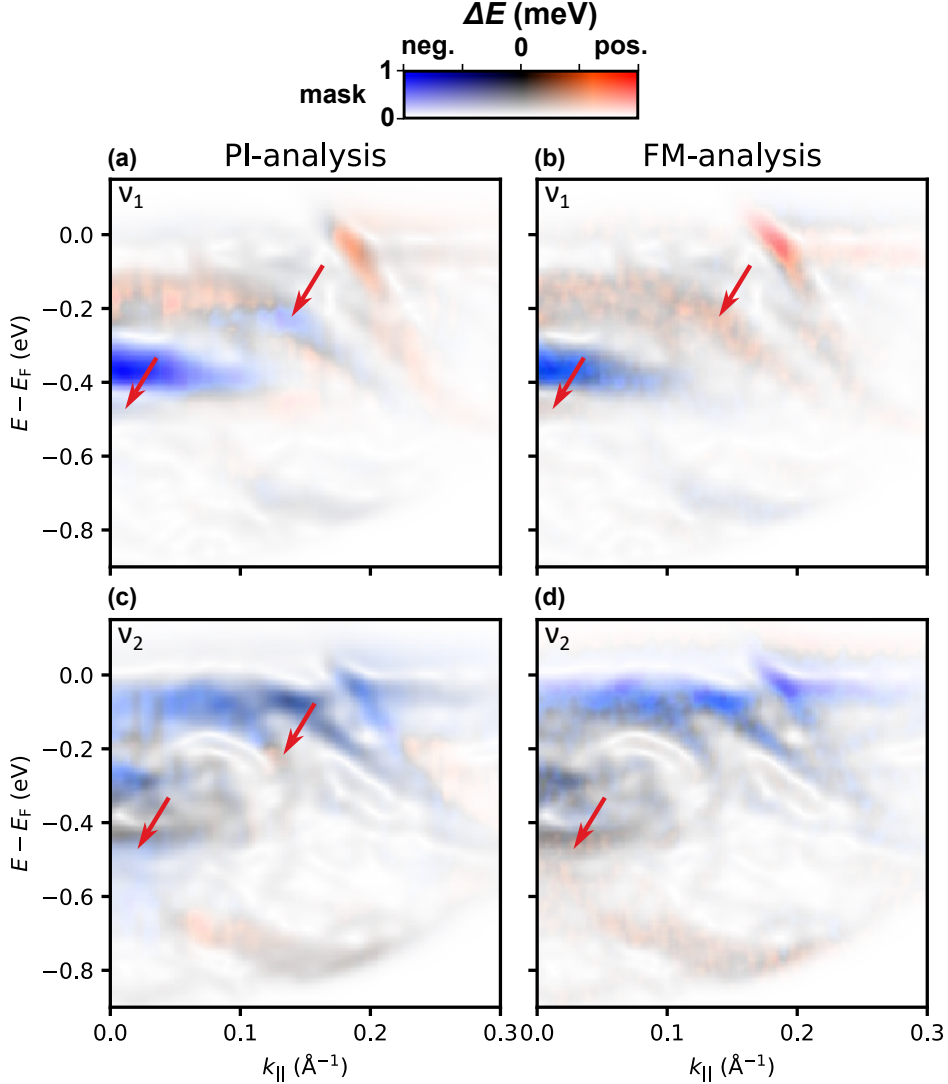
A. Theoretical Framework

For ultrafast dynamic simulations, the time-dependent Boltzmann equations, as recently implemented in EPW, are used to calculate the time-dependent electronic occupations $f_{n\mathbf{k}}(t)$ using the *ab initio* collision integrals for electron and phonon occupations: [4, 5]

$$\partial f_{n\mathbf{k}} = \Gamma^{\text{e-ph}}[f_{n\mathbf{k}}, n_{q\nu}] + \Gamma^{\text{e-e}}[f_{n\mathbf{k}}] \quad , \quad (\text{S2})$$

$$\partial n_{q\nu} = \Gamma^{\text{ph-e}}[f_{n\mathbf{k}}, n_{q\nu}] \quad , \quad (\text{S3})$$

where $n_{q\nu}$ denotes the phonon distribution function, and $\Gamma^{\text{e-ph}}$, $\Gamma^{\text{e-e}}$, and $\Gamma^{\text{ph-e}}$ the collision integrals due to electron-phonon, electron-electron, and phonon-electron scattering, respectively. The explicit expressions for the collision integrals can be found elsewhere. [4]



Supplementary Figure S4. Comparison between the results of the PI analysis [(a) and (c)] and FM analysis [(b) and (d)] of the experimental data for ν_1 and ν_2 . The band renormalizations are superimposed on the band structure masks shown in Fig. S3. The arrows indicate areas, where PI analysis and FM analysis show opposite signs for ΔE .

The time-dependent displacement amplitude Q_ν of the coherent phonon mode ν can be obtained by the solution of the coherent-phonon equation of motion: [6]

$$\partial_t^2 Q_\nu + \omega_\nu^2 Q_\nu = -\frac{2\omega_\nu}{\hbar} \sum_{\mathbf{nk}} g_{n\mathbf{k}}^\nu(\mathbf{k}, 0) \Delta f_{n\mathbf{k}}(t) \quad . \quad (\text{S4})$$

Here, ω_ν is the frequency of the coherent-phonon mode and $\Delta f_{n\mathbf{k}}(t) = f_{n\mathbf{k}}(t) - f_{n\mathbf{k}}^{(0)}$ is the change of the electronic occupations compared to the carrier distribution before photoexci-

tation $f_{n\mathbf{k}}^{(0)}$. The band renormalization mediated by the coherent phonons is given by:[7]

$$\Sigma_{n\mathbf{k}}^p(t) = \sum_{\nu} g_{nn}^{\nu}(\mathbf{k}, 0) Q_{\nu}(t) \quad . \quad (\text{S5})$$

The EPC matrix mediates the change of the eigenenergy that the nuclear motion imposes on the electronic system. The strength of our *ab initio* method lies in its ability to disentangle the contributions of each coherent-phonon mode to the momentum- and energy-resolved band renormalization individually, (as well as the momentum- and energy-resolved electronic contributions to the force acting on the atoms after photoexcitation).

The displacement amplitude can also be linked to the actual nuclear displacement by: [8]

$$\Delta\tau_{\kappa p} = \sum_{\mathbf{q}\nu} \left(\frac{\hbar}{2\omega_{\mathbf{q}\nu} M_{\kappa}} \right)^{\frac{1}{2}} e^{i\mathbf{q}\cdot\mathbf{R}_p} \mathbf{e}_{\mathbf{q}\nu}^{\kappa} Q_{\mathbf{q}\nu} \quad ,$$

where κ and p are the indices of the nucleus and unit cell, M_{κ} is the nuclear mass, $\mathbf{e}_{\mathbf{q}\nu}^{\kappa}$ is the phonon eigenvector and \mathbf{R}_p is the crystal-lattice vector.

B. Computational details

Density functional theory (DFT) calculations are performed with the plane-wave pseudopotential code `Quantum ESPRESSO` [9, 10], using fully-relativistic projector augmented wave (PAW) pseudopotentials [11] and the Perdew-Burke-Ernzerhof generalized-gradient approximation in solids (PBEsol) for the exchange-correlation functional [12]. The plane-wave kinetic-energy cutoff is set to 80 Ry, and the Brillouin zone (BZ) is sampled with a $10 \times 6 \times 4$ Monkhorst-Pack grid [13]. For the BZ integration, we used a Gaussian smearing with a spreading of 0.02 Ry to mimic an elevated temperature needed for the $1T'$ phase of MoTe_2 to emerge [14]. The lattice parameter of the monoclinic unit cell with the space group $P2_1/m$ determined through crystal structure and unit cell relaxation are $a = 3.457$, $b = 6.320$, $c = 13.694$ and $\beta = 91.8$, which agrees well with the experimental values [15]. The phonon dispersion is obtained from density functional perturbation theory (DFPT) on a $5 \times 3 \times 2$ q-point mesh [16]. The electron and phonon eigenvalues are interpolated and the electron-phonon coupling matrix $g_{mn}^{\nu}(\mathbf{k}, \mathbf{q})$ is calculated on a dense $30 \times 18 \times 12$ grid via maximally-localized Wannier functions [17] within the `EPW` code [18], which uses `Wannier90` as a library [19].

The joint time-dependent Boltzmann equations and the coherent-phonon equation of motion are propagated within an energy window of 1.5 eV around the Fermi energy. The time propagation is achieved using the second-order Runge-Kutta method over a total simulation time of 6 ps with a time stepping of 1 fs. The collision integrals (Eqs. S2-S3) are evaluated on the dense $30 \times 18 \times 12$ grid with a gaussian smearing of 10 meV. The lattice temperature is set to room temperature $T_{\text{lat}} = 300$ K and the electronic temperature T_e corresponding to the absorbed fluence of the experiment is estimated to be $T_e = 1325$ K according to the procedure described in [7]. For the electron-electron scattering, an average electron linewidth of 10 meV for the states within the energy window was chosen. For realistic comparison with the measurements, the experimental energy- and time-resolution were accounted for via Gaussian convolutions.

-
- [1] N. Gauthier, H. Soifer, J. A. Sobota, H. Pfau, E. J. Sie, A. M. Lindenberg, Z.-X. Shen, and P. S. Kirchmann, Analysis methodology of coherent oscillations in time-and angle-resolved photoemission spectroscopy, *Review of Scientific Instruments* **96** (2025).
- [2] P. Hein, S. Jauernik, H. Erk, L. Yang, Y. Qi, Y. Sun, C. Felser, and M. Bauer, Mode-resolved reciprocal space mapping of electron-phonon interaction in the weyl semimetal candidate *td-wte2*, *Nature communications* **11**, 2613 (2020).
- [3] I. Sobel, An isotropic 3x3 image gradient operator, Presentation at Stanford A.I. Project 1968 (2014).
- [4] F. Caruso and D. Novko, Ultrafast dynamics of electrons and phonons: from the two-temperature model to the time-dependent boltzmann equation, *Advances in Physics: X* **7**, 2095925 (2022).
- [5] Y. Pan and F. Caruso, Vibrational dichroism of chiral valley phonons, *Nano Letters* **23**, 7463 (2023).
- [6] F. Caruso and M. Zacharias, Quantum theory of light-driven coherent lattice dynamics, *Phys. Rev. B* **107**, 054102 (2023).
- [7] C. Emeis, S. Jauernik, S. Dahiya, Y. Pan, C. E. Jensen, P. Hein, M. Bauer, and F. Caruso, Coherent phonons and quasiparticle renormalization in semimetals from first principles, *Physical Review X* **15**, 021039 (2025).
- [8] F. Giustino, Electron-phonon interactions from first principles, *Rev. Mod. Phys.* **89**, 015003 (2017).
- [9] P. Giannozzi, S. Baroni, N. Bonini, M. Calandra, R. Car, C. Cavazzoni, D. Ceresoli, G. L. Chiarotti, M. Cococcioni, I. Dabo, *et al.*, *Quantum ESPRESSO*: a modular and open-source software project for quantum simulations of materials, *J. Phys. Condens. Matter* **21**, 395502 (2009).
- [10] P. Giannozzi, O. Andreussi, T. Brumme, O. Bunau, M. B. Nardelli, M. Calandra, R. Car, C. Cavazzoni, D. Ceresoli, M. Cococcioni, *et al.*, Advanced capabilities for materials modelling with *Quantum ESPRESSO*, *J. Phys. Condens. Matter* **29**, 465901 (2017).
- [11] A. Dal Corso, Pseudopotentials periodic table: From H to Pu, *Comput. Mater. Sci.* **95**, 337 (2014).

- [12] J. P. Perdew, A. Ruzsinszky, G. I. Csonka, O. A. Vydrov, G. E. Scuseria, L. A. Constantin, X. Zhou, and K. Burke, Restoring the density-gradient expansion for exchange in solids and surfaces, *Phys. Rev. Lett.* **100**, 136406 (2008).
- [13] H. J. Monkhorst and J. D. Pack, Special points for brillouin-zone integrations, *Phys. Rev. B* **13**, 5188 (1976).
- [14] E. Bosoni, L. Beal, M. Bercx, P. Blaha, S. Blügel, J. Bröder, M. Callsen, S. Cottenier, A. Degomme, V. Dikan, *et al.*, How to verify the precision of density-functional-theory implementations via reproducible and universal workflows, *Nature Reviews Physics* **6**, 45 (2024).
- [15] B. E. Brown, The crystal structures of wte2 and high-temperature mote2, *Acta Crystallographica* **20**, 268 (1966).
- [16] S. Baroni, S. De Gironcoli, A. Dal Corso, and P. Giannozzi, Phonons and related crystal properties from density-functional perturbation theory, *Reviews of Modern Physics* **73**, 515 (2001).
- [17] N. Marzari, A. A. Mostofi, J. R. Yates, I. Souza, and D. Vanderbilt, Maximally localized Wannier functions: Theory and applications, *Reviews of Modern Physics* **84**, 1419 (2012).
- [18] H. Lee, S. Poncé, K. Bushick, S. Hajinazar, J. Lafuente-Bartolome, J. Leveillee, C. Lian, J.-M. Lihm, F. Macheda, H. Mori, *et al.*, Electron-phonon physics from first principles using the EPW code, *npj Computational Materials* **9**, 156 (2023).
- [19] G. Pizzi, V. Vitale, R. Arita, S. Blügel, F. Freimuth, G. Géranton, M. Gibertini, D. Gresch, C. Johnson, T. Koretsune, *et al.*, **wannier90** as a community code: new features and applications, *Journal of Physics: Condensed Matter* **32**, 165902 (2020).